

A Particle-Water Based Model for Water Retention Hysteresis

Yixiang Gan^a, Federico Maggi^a, Giuseppe Buscarnera^b, Itai Einav^a

^a*School of Civil Engineering, The University of Sydney, NSW 2006, Australia*

^b*Department of Civil and Environmental Engineering, Northwestern University, Evanston, IL 60208, United States*

Abstract

A particle-water discrete element-based approach to describe water movement in partially saturated granular media is presented and tested. Water potential is governed by both capillary bridges, dominant at low saturations, and pressure of entrapped air, dominant at high saturations. The approach captures the hysteresis of water retention during wetting and drainage by introducing local evolution of liquid-solid contact angles at the level of pores and grains. Next, extensive comparisons against experimental data are presented. While this is made without involving any fitting parameters, the method demonstrates relative high success by achieving a correlation coefficient of at least 82%, and mostly above 90%.

Keywords: water retention; hysteresis effects; discrete element method; partially saturated granular materials

1. Introduction

Water retention in partially saturated soil is fundamental in soil mechanics [1, 2, 3, 4], and has important implications in soil ecohydrology [5] as well as nutrient cycle and microbial ecology [6, 7]. Of particular interest in the past decades has been to address water management in agriculture [8, 9, 10], contaminant flow [11, 12, 13, 14], bio- and phytoremediation [15, 16], and water treatment [17, 18].

The water retention relation between water potential and degree of saturation is typically used to define the hydraulic behaviour of soils. A key element of this relation is the hysteresis observed during cycles of wetting and drainage. Water retention hysteresis in soils may be ascribed to: (1) geometric or ink-bottle effects; (2) differences in contact angles during wetting and drying; (3) entrapment of non-wetting-phase (e.g., gas, oil, etc.); and (4) shrinking and swelling of pores [19, 20, 21, 22].

The overall behaviour of partially saturated soils depends on the solid skeleton, the way liquids and gases are connected, and the way forces interact along interfaces. Soil properties can be characterized by the pore size distribution [23, 24], and by the distributions of grain sizes and shapes [8, 9]. The interfaces between the solid, liquid and gaseous phases can be characterized by the grain surface profiles, their hydrophilicity, and thermodynamic properties [25, 26, 27, 28].

Existing phenomenological models parameterise the water retention curve using parameters that do not necessarily have a direct physical meaning [29, 30, 9]. For example, two sets of parameters are to be determined for the van Genuchten equation to reproduce the water retention curve during drainage and wetting, yet there is no consensus on what these two sets of parameters mean. What may be relevant is to establish an explanation that would bypass such phenomenology and thus highlight what actually happens at the grain scale and at the interfaces between solids, liquids and gases.

Numerical modelling of water flow and the resulting retention is feasible with the aid of Discrete Element Methods (DEM) [31], but this has not yet revealed water retention hysteresis, at least not a quantitatively successful way. Nevertheless, DEM has been used to describe inter-granular capillary interactions at low water saturations (i.e., for continuous gas and discontinuous liquid, or the pendular state) [24, 32, 33, 34, 35, 36]; an extension of the DEM was proposed to incorporate intermediate saturations (i.e., for continuous gas and liquid phases, or the funicular state) [37, 38, 35], and full saturation (i.e., for continuous liquid and discontinuous gas, or the capillary state). However, only the coupling between these approaches would

allow to capture in full the retention curve of partially saturated soils during wetting and drying. Moreover, the coupling of these requires a scheme that extends beyond the capabilities of each of these individual frameworks, and that allows for model testing and validation against experimental observations of water retention, including hysteresis features.

The aim of this study is to develop a new DEM model for partially saturated granular materials, which is coupled with a newly-developed homogenisation scheme designed to connect local and averaged water potentials. The DEM model is based on the description of local water movement between neighbouring cells, each containing a single grain. The homogenisation scheme is used to determine the water retention curve, hence the relation between the averaged water potential against the averaged degree of saturation. The proposed homogenisation scheme is capable of describing partial saturation, and is specifically used to detect hydraulic hysteresis during wetting and drainage. The DEM model is tested for hysteresis cycles against three sets of experiments having variable grain size distribution, surface tension between phases, and contact angles.

2. Grain-scale properties

Grain-scale properties are defined in relation to tessellated cells. The boundaries of the i -th tessellated cell is obtained using a modified Voronoi tessellation method [39], where the i -th cell volume V_i^{cell} is centred around the corresponding grain. The total volume, V^{total} , is equal to the sum of V_i^{cell} , and each cell i is associated with a cell solid volume V_i^{grain} , water volume V_i^{water} and void volume $V_i^{\text{void}} = V_i^{\text{cell}} - V_i^{\text{grain}}$. Hence, the volumes at the scale of the domain are $V^{\text{void}} = \sum_i V_i^{\text{void}}$, $V^{\text{water}} = \sum_i V_i^{\text{water}}$ and $S_r = V^{\text{water}}/V^{\text{void}}$.

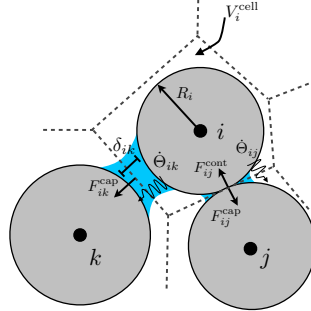


Figure 1: Schematics of three grains (grains' centres indicated by i , j and k) with connecting capillary bridges. The space has been divided using Voronoi tessellation, and water volumes within the cells vary by mass flux through cell boundaries, as $\dot{\Theta}_{ij}$ and $\dot{\Theta}_{ik}$.

The degree of saturation, porosity, and water content of the i -th cell are defined by

$$S_{r,i} = \frac{V_i^{\text{water}}}{V_i^{\text{void}}} , \phi_i = \frac{V_i^{\text{void}}}{V_i^{\text{cell}}} , \Theta_i = \frac{V_i^{\text{water}}}{V_i^{\text{cell}}} . \quad (1)$$

Capillary pressure due to the presence of a water meniscus between two grains adds to inter-granular forces in this DEM, which is calculated using an approximate solution to the Young-Laplace equation as a function of the radii of grains i and j (R_i and R_j), the gap distance (δ_{ij}), water volume of the capillary bridge, (V_{ij}^{br}), surface tension (γ), and the contact angle between water and grain (θ) [i.e., 40].

An important new aspect of the current method acknowledges the evolution of the contact angle θ between physically-meaningful minimum and maximum values (θ_{\min} and θ_{\max}) when the water bridge recedes or expands, respectively. The rate of change in contact angle is assumed to take the following form

$$\dot{\theta} = \alpha \frac{\dot{V}_{ij}^{\text{br}}}{R_{\text{eff}}^3} , \quad \text{and } \theta_{\min} \leq \theta \leq \theta_{\max} , \quad (2)$$

where \dot{V}^{br} is the rate of change of water volume of this capillary bridge, α is a non-dimensional coefficient controlling the dependence of the contact angle to the change of local water volume, and R_{eff} is the effective radius $R_{\text{eff}} = 2R_i R_j / (R_i + R_j)$. For a given pair of liquid and solid surface, the actual values of θ_{\min} and θ_{\max} depend not only on the chemical properties of the solid grain, but also on its surface morphology. These dynamics of θ between θ_{\min} and θ_{\max} is later shown to help us capturing hysteresis response during wetting and drainage (see also Fig. 2).

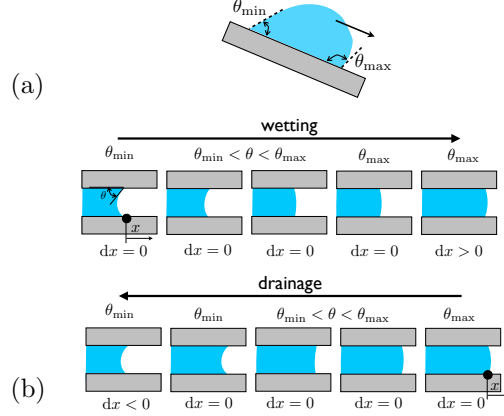


Figure 2: Schematics of contact angle dynamics: (a) Contact angle limits, shown for a water drop sliding along a tilted surface. (b) Contact angle dynamics during wetting and drainage.

Above a local critical degree of saturation, S_r^c , pressure due to entrapment of gas bubbles is introduced. The local critical degree of saturation S_r^c may depend on the grain's morphology through its fractal surface and it may be related to the air entry value in terms of saturation [41], but details will not be discussed here.

Assuming that the moles of gas, n , and temperature, T , are constant, then according to the ideal gas law, $u_p^a V_p^a = nRT$ (superscript a denotes the air-gas phase, where subscript p denotes an association to a particle-cell), the relative air pressure can be calculated as

$$\Delta u_p^a = u_p^a - u^a = \begin{cases} 0 & \text{if } S_r \leq S_r^c \\ \frac{S_r - S_r^c}{1 - S_r^c} u^a & \text{if } S_r > S_r^c \end{cases}, \quad (3)$$

where u^a and u_p^a are the atmospheric and particle-cell air pressures, respectively. The entrapped air volume is defined through S_r^c , as $V_0^{\text{air}} = (1 - S_r^c) V^{\text{void}}$. Note that according to the last relation S_r avoids to approach unity with increasing relative air pressure due to denominator approaching zero, with liquid tending to move to neighbouring cells.

3. Homogenisation scheme

A homogenisation scheme is next proposed to determine collective water potential in terms of local quantities. According to a common definition in partially saturated soil mechanics, the effective stress (σ'_{ij}) is related to the net stress tensor $\sigma_{ij}^{\text{net}} = \sigma_{ij} - u^a \delta_{ij}$, water pressure (u^w) and atmospheric air pressure (u^a) using [42]

$$\sigma_{ij}^{\text{net}} = \sigma'_{ij} - S_r \psi \delta_{ij}, \quad (4)$$

where $\psi = u^a - u^w$ is the water potential, and δ_{ij} is the Kronecker delta. Note that for saturations above S_r^c the particle-cell air pressure u_p^a is not the atmospheric air pressure u^a at saturations (see Eq. (3)).

Scholtes et al. [33] separates the net stress tensor into effective and capillary stress tensors,

$$\langle \sigma \rangle_{ij}^{\text{net}} = \langle \sigma \rangle'_{ij} + \langle \sigma \rangle_{ij}^{\text{cap}} = \frac{1}{V} \left(\sum_c F_i^{\text{cont}} x_j + \sum_c F_i^{\text{cap}} x_j \right),$$

where \mathbf{x} is the centre-to-centre vector between two neighbouring grains, with the contact and capillary forces defined by \mathbf{F}^{cont} and \mathbf{F}^{cap} , respectively. The expression $\langle \cdot \rangle$ indicates a volume average. A more general equilibrium equation should introduce forces due to relative air pressure,

$$\begin{aligned}\langle \sigma \rangle_{ij}^{\text{net}} &= \langle \sigma \rangle'_{ij} + \langle \sigma \rangle_{ij}^{\text{cap}} + \langle \sigma \rangle_{ij}^{\text{air}} \\ &= \frac{1}{V} \left(\sum_c F_i^{\text{cont}} x_j + \sum_c F_i^{\text{cap}} x_j + \sum_p \Delta u_p^a V_p^{\text{cell}} \delta_{ij} \right),\end{aligned}\quad (5)$$

where we correlate the effective stress tensor, $\langle \sigma \rangle'_{ij}$ to the inter-granular contact forces, the capillary stress tensor $\langle \sigma \rangle_{ij}^{\text{cap}}$ to the capillary forces, and the intrinsic particle-cell air pressure $\langle \sigma \rangle_{ij}^{\text{air}}$ to the relative air pressures. A comparison of Eq. (4) with Eq. (5) shows the following trace of stress tensors

$$\langle \sigma \rangle_{ii}^{\text{cap}} + \langle \sigma \rangle_{ii}^{\text{air}} = -3S_r \psi.$$

Thus, the water potential ψ can be stated in terms of homogenised quantities,

$$\psi = -\frac{1}{3S_r V} \left(\sum_c F_i^{\text{cap}} x_i + \sum_p \Delta u_p^a V_p^{\text{cell}} \right), \quad (6)$$

The second term of Eq. (6) is negligible at low saturation, while the first is negligible near saturation. Note that this homogenisation scheme may be included in systems with more than one component per phase [43].

The rate of change of the water content (in the cell scale $\Theta_i = V_i^{\text{water}}/V_i^{\text{cell}}$) can be calculated with the Richards equation [29],

$$\frac{\partial \Theta}{\partial t} = \nabla \left[K(\Theta) \nabla (\psi + \rho g z) \right]. \quad (7)$$

where $K(\Theta)$ is the hydraulic conductivity, and z is the vertical position. The (cell) volume integral of Eq. (7) can be written as the circuitation on the cell boundary using the Green's theorem as:

$$\int \frac{\partial \Theta}{\partial t} dV = - \oint \Phi \cdot \mathbf{n} dS, \quad (8)$$

where \mathbf{n} is the surface normal, $\Phi = -K(\Theta) \nabla (\psi + \rho g z)$ is the water flux, and ψ is determined as in Eq. (6) for each cell. The change of local water volume can be calculated using the individual fluxes between its neighbouring grains, through the discrete version of Eq. (8),

$$\begin{aligned}\Delta V_i^{\text{water}} &= V_i^{\text{cell}} \cdot \Delta \Theta = - \sum_j \Phi_{ij}^{\text{water}} A_{ij} \Delta t, \\ \Phi_{ij}^{\text{water}} &= -\frac{K_0}{|\mathbf{x}_j - \mathbf{x}_i|} \left[\psi_j - \psi_i + \rho g (z_j - z_i) \right].\end{aligned}\quad (9)$$

We assume that changes of cell volume are negligible during each time iterations, i.e., $\Delta V_i^{\text{cell}} \approx 0$. Note also that we assume that the hydraulic conductivity between adjacent cells is a function of the product between a constant conductivity per unit surface area K_0 and the conduction area A_{ij} (the 'wet' area along a Voronoi interface), which corresponds to the cross-sectional area of the water bridge along at the boundary between two cells. As compared to the hydraulic conductivity in Eq. (7), this approach allows us to set down a flow equation relatively simple while retaining the proportionality between ease of water movement and level of wetness, i.e., Darcian water velocity is greater as the medium is wetter. Within each cell, the total water volume is distributed to multiple existing water bridges [40]; the time for redistribution within the cell is considered to be negligible as compared to the time needed for water to move to connected cells.

4. Simulation results and discussion

Initial and boundary conditions

We use a three-dimensional simulation domain consisting of 2,500 grains. The grains are nearly mono-sized with 5% variation in diameter. The mechanical boundary conditions are periodic for grain dynamics. An initial porosity $\phi = 37\%$ is being achieved by a stage of pre-compaction from a looser state. This corresponds to a close packing state for nearly mono-sized spherical grains. For this configuration, the grain motion during the processes is negligible and the pore size distribution across the sample is nearly uniform. During simulations the domain volume is fixed, i.e., constant porosity. The hydraulic boundary conditions involve water inflow through a constant positive water pressure difference from the top during wetting, and a water outflow through a constant negative water pressure difference from the bottom during drainage. The wetting and drainage processes are applied to complete a scanning cycle between predefined maximum and minimum saturations for the whole simulation domain. The collective water potential, ψ , is calculated using Eq. (6). The parameters used in this study can be found in Table 1. The units in the simulations are not listed, but their magnitude is inspired by the later results related to the experimental data, where units are relevant.

Table 1: Model parameters used in the simulations.

Variable	Symbol	Value
grain size	d	1.0 ± 0.05
porosity	ϕ	37%
surface tension	γ	0.01
hydraulic conductivity	K_0	5.0
contact angle coefficient	α	10.0
saturation for air entrapment	S_r^c	0.98
atmospheric air pressure	u^a	0.01
elastic modulus of grains	E	1000

Hysteresis with contact angle dynamics

Three sets of numerical analyses have been performed to show retention hysteresis predicted by the model and its dependency on the contact angle dynamics using: (1) various fixed contact angles, (2) the scanning window across various degrees of saturation, and (3) various combinations of receding and advancing angles, θ_{\min} and θ_{\max} .

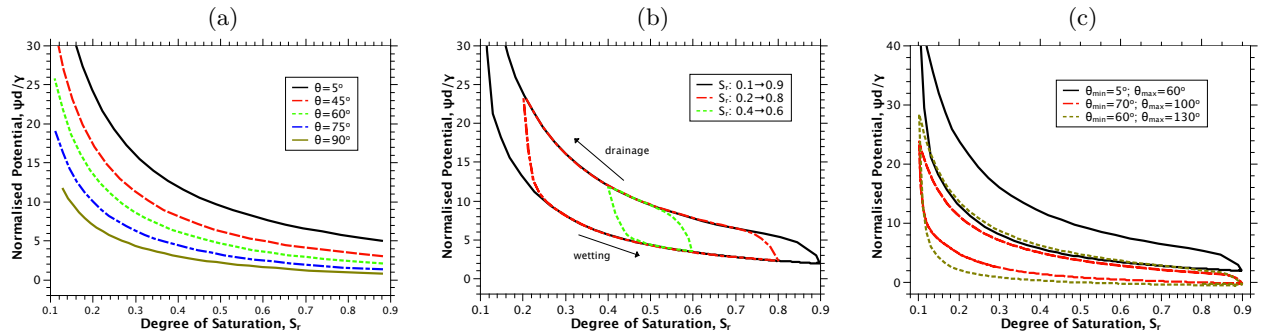


Figure 3: Water retention curves: (a) fixed contact angles, (b) hysteresis using $\theta_{\min} = 5^\circ$ and $\theta_{\max} = 60^\circ$ for different scanning windows, (c) hysteresis for different pairs of receding and advancing angles. The arrows in (b) show the directions of drainage and wetting processes.

Table 2: Properties of the experimental systems*.

carried out by	system	contact angle θ (°)	density ρ (kg/m ³)	surface tension γ (N/m)	diameter d (mm)	eff. diameter \bar{d} (mm)**
Heinse et al. [9]	Profile	5–60 [19]	1000	0.073	0.25–1.0	0.7
	Turf	5–60 [19]	1000	0.073	1.0–2.0	1.5
	Mix	5–60 [19]	1000	0.073	0.25–2.0	1.0
Dury et al. [11]	Water	5–60 [19]	1000	0.07025	0.08–1.2	0.27
	2% Butanol	5–60 [19]	996	0.04405	0.08–1.2	0.27
	6% Butanol	5–60 [19]	989	0.03075	0.08–1.2	0.27
Culligan et al. [13]	Water-Soltrol	72–105 [44]	1000	0.0378 [45]	0.6–1.4	0.85

* The properties listed were reported by the authors carrying out the tests, unless otherwise stated.

** Effective diameter values used for the comparisons against the simulations.

We first use fixed contact angles, as $\theta_{\min} = \theta_{\max} = 5^\circ, 45^\circ, 60^\circ, 75^\circ, 90^\circ$, to show the sensitivity of the water retention to θ in Fig. 3(a). The water potential is normalised as $\bar{\psi} = \psi \bar{d} / \gamma$, where \bar{d} is the effective diameter for the system. This normalisation captures the effects of grain size and surface tension γ . In simulations, the effective diameter is the mean diameter of the grains. By using a fixed contact angle θ for these mono-sized systems, the retention curves do not demonstrate hysteresis for the scanning between $S_r = 0.1$ and 0.9 .

The next example involves contact angle dynamics between $\theta_{\min} = 5^\circ$ and $\theta_{\max} = 60^\circ$. There are three cases of hysteresis, for scanning between $0.1 \leq S_r \leq 0.9$, $0.2 \leq S_r \leq 0.8$, and $0.4 \leq S_r \leq 0.6$ (Fig. 3(b)). The shape of the envelope of the scanning curves is determined by the dynamics of contact angles. In the transition between drainage and wetting, the distribution of local contact angles determines the water retention relations between the water potential and the saturation (later shown in Fig. 8). The dynamics of the contact angle embedded in Eq. (2) holds the key for our model’s ability to separate wetting and drainage branches of the hysteresis cycle. The shape of the hysteresis during transitions from drainage to wetting (and vice versa) is influenced by this equation, as we observed sensitivity to the parameter α . The homogenised water potential $\bar{\psi}$ increases during drainage, due to increase in F^{cap} and decrease in S_r , as reflected by Eq. (6).

Fig. 3(c) shows overall responses of three systems using different pairs of receding and advancing angles, namely, $(\theta_{\min}, \theta_{\max}) = (5^\circ, 60^\circ)$, $(70^\circ, 100^\circ)$, $(60^\circ, 130^\circ)$. The combination of θ_{\min} and θ_{\max} controls the shape and position of the retention hysteresis.

Comparison to experiments

The model predictions are compared with experimental data from the existing literature to investigate three aspects that influence the overall retention hysteresis: grain size [9], surface tension [11], and pair receding and advancing angles [13]. Table 2 summarises the grain properties of these experiments, which are also directly used in the simulations.

In the first set of experiments, Heinse et al. [9] measured the water retention hysteresis in granular materials composed of different sized aggregates. Fig. 4 shows the comparison between the simulated hysteresis with the experimental data [9]. For model-to-experiment comparison, we use the absolute matric potential, $\psi/(\rho g)$, and water content, Θ , for samples having different grain size distributions (Fig. 4(a)-(c)). In Fig. 4(d), the experimental data are represented using a normalised potential $\bar{\psi} = \psi \bar{d} / \gamma$ and effective degree of saturation $S_r^{\text{eff}} = (\Theta - \Theta_{\min}) / (\Theta_{\max} - \Theta_{\min})$. The use of the normalised $\bar{\psi}$ makes the evaluation independent from the grain size. We calculated the correlation coefficients (r_c) between our predictions and experimental data for wetting and drainage branches, separately, from all three cases. The correlation coefficients for the wetting branches range from 0.90 to 0.94 and are higher than the ones obtained from the drainage branches, which range from 0.86 to 0.89. Note that this comparison did not involve any fitting parameters in the DEM simulations: this is therefore an *ab initio* comparison between numerical predictions and experiments. In general, the predictions for wetting branch are better than the ones for the drainage

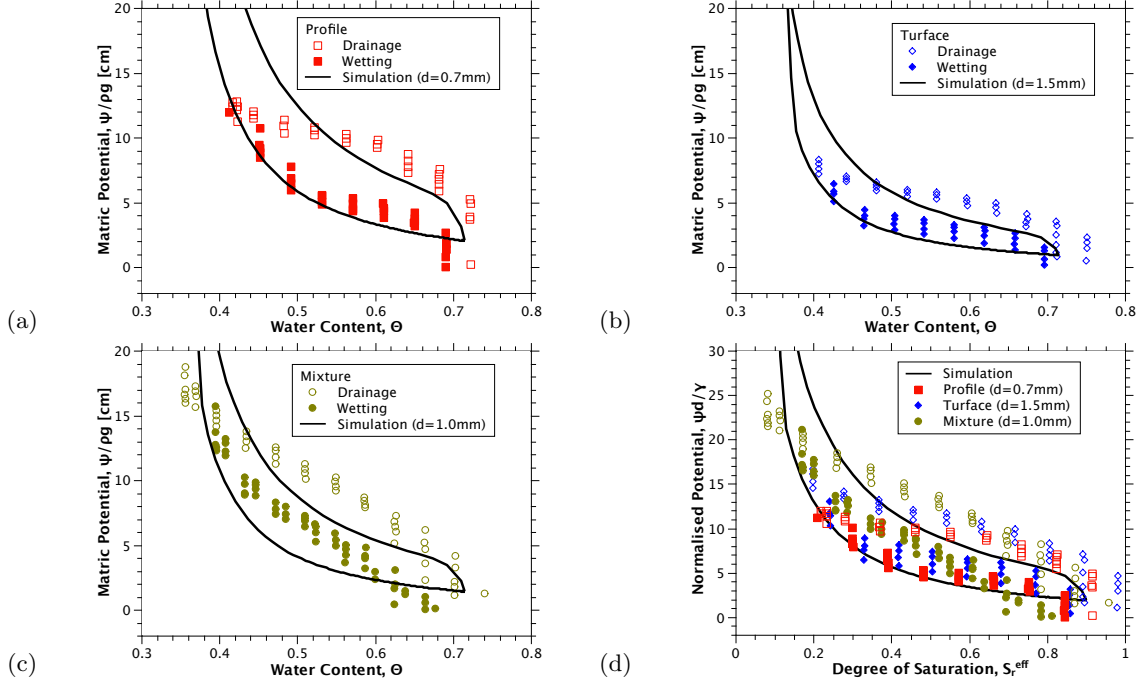


Figure 4: Comparison between simulated water retention curves and experimental data: (a) Profile (b) Turface (c) Mixture (d) Normalised data. The experimental data are normalised with the density ρ , effective grain size \bar{d} , and surface tension γ , listed in Table 2. We use $\Theta_{\min} = 0.32$, $\Theta_{\max} = 0.75$ to convert the water content to the effective degree of saturation [8].

branches. The predictions of water potential for the drainage branch at low saturation are usually higher than the measured values, possibly because the simulations were initially closely-packed and thus inhibiting grain motion as compared to the experimental systems.

In the second set of experiments, Dury et al. [11] used various water-butanol mixtures at 0%, 2% and 6% to alter the liquid surface tension. These wetting liquids were used to measure the corresponding capillary pressure-saturation relations. Similarly to Fig. 4, Fig. 5(a)-(c) show the comparisons between the predicted and experimental hysteresis in the space of matric potential and degree of saturation, and being normalised in Fig. 5(d). The calculated correlation coefficients ranges between 0.93 and 0.98 for wetting branches, and for drainage, between 0.82 and 0.98.

In the third set of experiments used for comparison, Culligan et al. [13] employed a water-Soltrol 220 system in glass beads. Unlike the previous two sets of experiments, where the void is occupied by air, here "void" represents the volume taken by the oil phase in the oil-water system. As a result, the contact angle in this case is the one between water and oil, and the corresponding value can be found in Table 2. Fig. 6(b) shows the comparison of our model prediction with data from Culligan et al. [13] for the oil-water system. Using X-ray micro-tomography, Culligan et al. [13] further confirmed that in the sample the water saturation (S_r) and oil saturation ($1 - S_r$) levels were rather homogeneous along the gravity direction. From the modelling perspective, the main differences between the air-water and oil-water systems are (1) advancing and receding contact angles, (2) surface tension between the wetting liquid and "void"; (3) the compressibility of the "void", as in Eq. (3). Using normalised capillary potential, Fig. 6(a) and (b) demonstrate the difference by using corresponding advancing and receding angles for air-water and oil-water systems. The correlation coefficient for wetting is 0.82, and for drainage 0.93.

Grain scale information

The proposed method is advantageous in offering insights into local grain-scale informations, such as distributions of local water contents and potential during the wetting-drainage cycles. Fig. 7 presents six

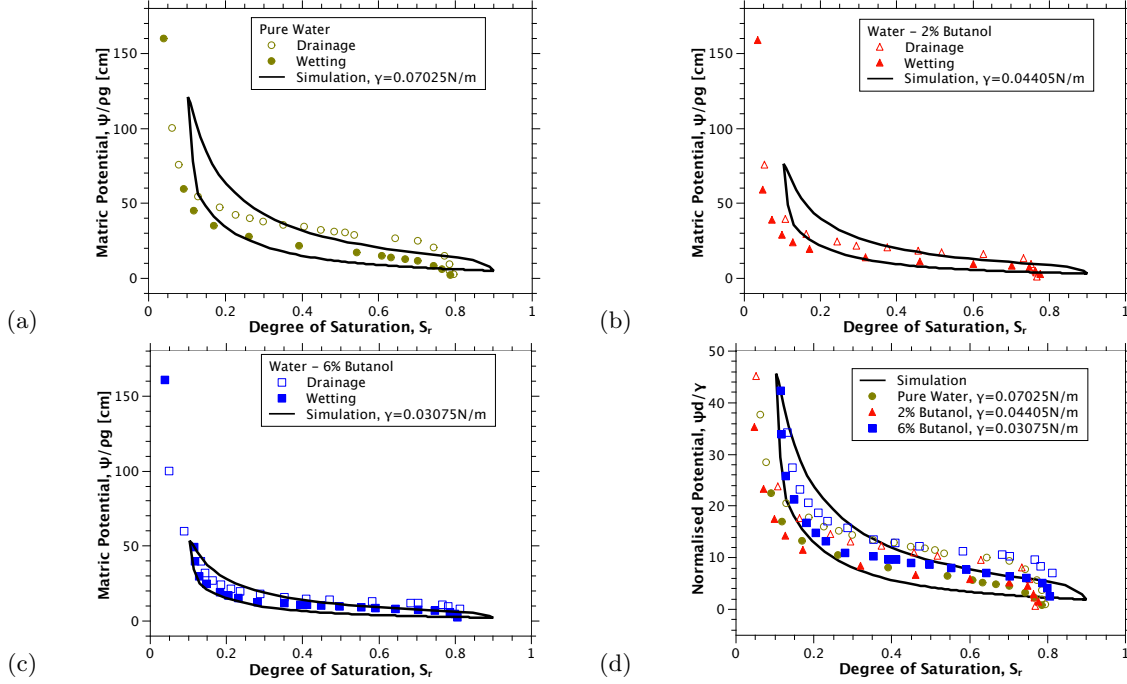


Figure 5: Comparison between simulated retention curves and experimental data from Dury et al. [11]: (a) Water (b) 2% Butanol (c) 6% Butanol (d) Normalised data. The experimental data are normalised with the density ρ , effective grain size \bar{d} , and surface tension γ , listed in Table 2.

temporal snapshots of spatial-distributed water content and the probability distribution of stress components, capillary and air stresses, for each cell between $0.1 \leq S_r \leq 0.9$. It is relevant to compare snapshot pairs (a) and (f), (b) and (e), and (c) and (d), corresponding to drainage and wetting, respectively. Overall, it is found that probability of high capillary stresses is higher during drainage, which explains the difference in the overall matrix potential. Furthermore, the entrapped particle-cell air pressures is only present at higher saturations, but this is rather symmetrical during drainage and wetting, and can therefore not be attributed to explain the hysteresis. This is expected, since Eq. (3) is associated only to high degrees of saturation.

In this study, water retention hysteresis has been connected to the contact angle dynamics *via* Eq. (2). Therefore, it is useful to plot the distributions of individual contact angles during wetting and drainage. Fig. 8 shows the contact angle distribution and its evolution during transitions between drainage and wetting processes, at stages shown in Fig. 6(a). This demonstrates how the distribution of contact angles inside the sample determines the overall water potential, and thus provides an explanation for different water retention curves for wetting and drainage processes.

Future work will include sensitivity analyses to the effects of grain size distribution, porosity and hydraulic conductivity. The current study illustrates the role of the contact angle dynamics in controlling the water retention hysteresis, but the method should enable to study the effects of grain motion and pore size distribution on retention hysteresis.

5. Conclusions

We proposed a computational DEM model of the retention of fluids during wetting and drainage in partially saturated granular materials. By supporting this method with a new homogenisation scheme, and employing grain-level quantities of water content and potential, this study demonstrates how small-scale hydro-mechanical parameters and variables control the phenomenology of larger-scale water retention.

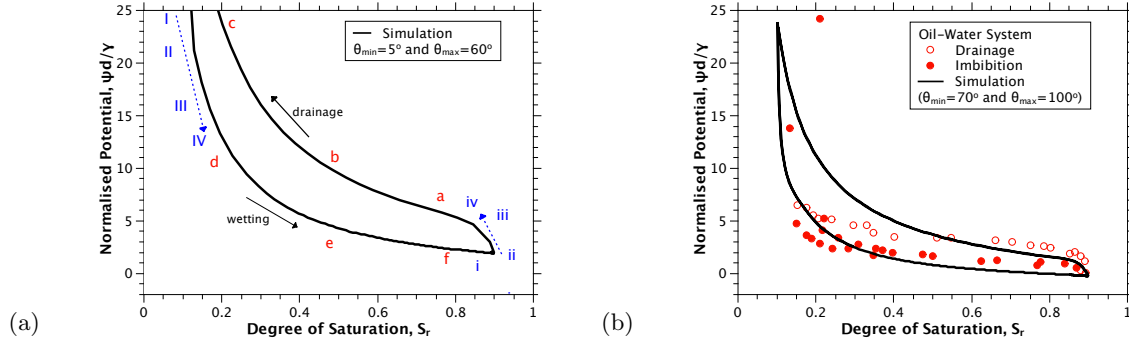


Figure 6: Retention hysteresis curves with (a) $\theta_{\min} = 5^\circ$ and $\theta_{\max} = 60^\circ$, and (b) $\theta_{\min} = 70^\circ$ and $\theta_{\max} = 100^\circ$. In (a), the symbols (a to b) and numbers (i to iv, and I to IV) indicated the cases for plotting water distribution later in Fig. 7 and Fig. 8, respectively. In (b), the model prediction is compared to experimental data from Culligan et al. [13] for the oil-water system.

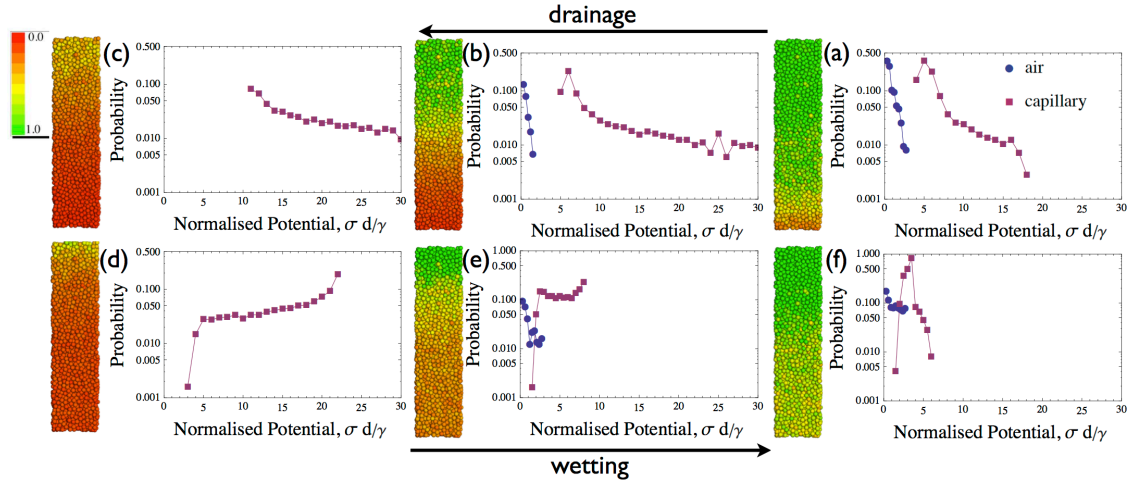


Figure 7: Water distribution and grain-scale stress components in six stages, (a) to (c) for drainage, and (d) to (f) for wetting, referred to Fig. 6(a). Each stage contains one profile and one probability distribution. Profiles show the local water distribution coloured by the degree of saturation with the scale between 0 and 1. Also shown are probability distributions of the magnitudes of particle-cell air and capillary stress components (σ^{air} and σ^{cap} , respectively).

Within the context of this study, a major finding was that the hysteresis of water retention during cycles of wetting and drainage has been shown to arise from the dynamics of the solid-liquid contact angles as a function of the change of the local water volumes. The comparison with experiments from different sources highlights the relative success of our model by directly involving only physical-based micro-scale hydro-mechanical properties.

Acknowledgement

Financial support for this research from the Australian Research Council through Grant No. DP120104926 and DE130101639 is gratefully appreciated. The authors would like to thank Dr. Jean-Michel Pereira for his critical comments. The DEM code and scripts for the present study can be downloaded from <https://github.com/ganyx/CapDEM>.

- [1] B. Loret and N. Khalili. An effective stress elasticplastic model for unsaturated porous media. *Mechanics of Materials*, 34(2):97–116, 2002.
- [2] Mathieu Nuth and Lyesse Laloui. Advances in modelling hysteretic water retention curve in deformable soils. *Computers and Geotechnics*, 35(6):835–844, 2008.

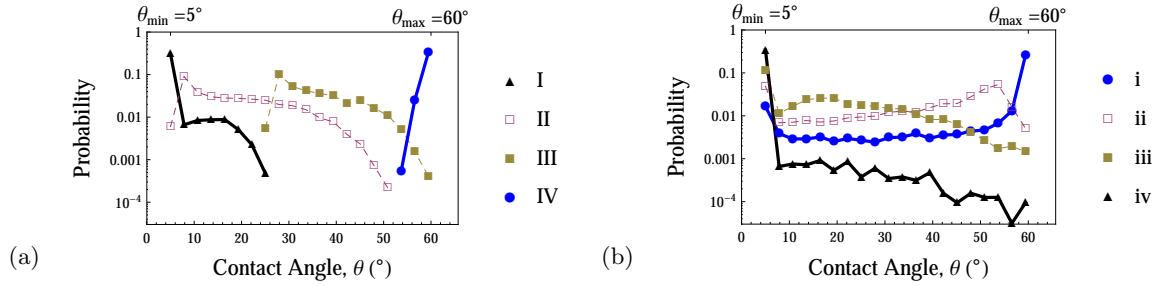


Figure 8: Probability distribution of contact angle for individual capillary bridges during (a) transition from drainage to wetting and (b) from wetting to drainage. Stages, I to IV and i to iv, are identified in Fig. 6(a).

- [3] D Sheng, a Gens, D Fredlund, and S Sloan. Unsaturated soils: From constitutive modelling to numerical algorithms. *Computers and Geotechnics*, 35(6):810–824, 2008.
- [4] G. Buscarnera and I. Einav. The yielding of brittle unsaturated granular soils. *Géotechnique*, 62(2):147–160, 2012.
- [5] F Laio, A Porporato, L Ridolfi, and I Rodriguez-Iturbe. Plants in water-controlled ecosystems: Active role in hydrologic processes and response to water stress: II. Probabilistic soil moisture dynamics. *Advanced Water Resources*, 24(7):707723, 2001.
- [6] J W Crawford, J A Harris, K Ritz, and I M Young. Towards an evolutionary ecology of life in soil. *Trends in Ecology and Evolution*, 20(2):8187, 2005.
- [7] F Maggi, C Gu, W J Riley, G M Hornberger, R T Venterea, T Xu, N Spyker, N L Miller, and C M Oldenburg. A mechanistic treatment of the dominant soil nitrogen cycling processes: Model development, testing, and application. *Journal of Geophysical Research: Biogeosciences*, 113:G02016, 2008.
- [8] J. M. Blonquist, S. B. Jones, I. Lebron, and D. Robinson. Microstructural and phase configurational effects determining water content: Dielectric relationships of aggregated porous media. *Water Resources Research*, 42(5):1–13, 2006.
- [9] Robert Heinse, Scott B. Jones, Susan L. Steinberg, Markus Tuller, and Dani Or. Measurements and Modeling of Variable Gravity Effects on Water Distribution and Flow in Unsaturated Porous Media. *Vadose Zone Journal*, 6(4):713, 2007.
- [10] Chuanhui Gu, F. Maggi, W. J. Riley, G. M. Hornberger, T. Xu, C. M. Oldenburg, N. Spyker, N. L. Miller, R. T. Venterea, and C. Steefel. Aqueous and gaseous nitrogen losses induced by fertilizer application. *Journal of Geophysical Research*, 114(G1):G01006, 2009.
- [11] O. Dury, U. Fischer, and R. Schulin. Dependence of hydraulic and pneumatic characteristics of soils on a dissolved organic compound. *Journal of Contaminant Hydrology*, 33(1-2):39–57, 1998.
- [12] J. I. Gerhard and B. H. Kueper. Capillary pressure characteristics necessary for simulating DNAPL infiltration, redistribution, and immobilization in saturated porous media. *Water Resources Research*, 39(8):1212, 2003.
- [13] Katherine A. Culligan, Dorth Wildenschild, Britt S. B. Christensen, William G. Gray, Mark L. Rivers, and Andrew F. B. Thompson. Interfacial area measurements for unsaturated flow through a porous medium. *Water Resources Research*, 40(12):W12413, 2004.
- [14] RF Serrano, M Iskander, and K Tabe. 3D contaminant flow imaging in transparent granular porous media. *Géotechnique Letters*, 1:71–78, 2011.
- [15] D E Salt, R D Smith, and I Raskin. Phytoremediation. *Annual Review of Plant Physiology and Plant Molecular Biology*, 49:643668, 1998.
- [16] E Pilon-Smits. Phytoremediation. *Annual Review of Plant Biology*, 49:1539, 2005.
- [17] Lance C Schideman, Benito J Mariñas, Vernon L Snoeyink, and Carlos Campos. Three-component competitive adsorption model for fixed-bed and moving-bed granular activated carbon adsorbers. Part I. Model development. *Environmental Science & Technology*, 40(21):6805–11, 2006.
- [18] Matthew L Magnuson and Thomas F Speth. Quantitative structure–property relationships for enhancing predictions of synthetic organic chemical removal from drinking water by granular activated carbon. *Environmental Science & Technology*, 39(19):7706–11, 2005.
- [19] N Morrow. Capillary pressure correlations for uniformly wetted porous media. *Journal of Canadian Petroleum Technology*, pages 49–69, 1976.
- [20] James A Tindall, James R Kunkel, and Dean E Anderson. *Unsaturated zone hydrology for scientists and engineers*. Prentice Hall Upper Saddle River, New Jersey, 1999.
- [21] Katja Lappalainen, Mikko Manninen, Ville Alopaeus, Juhani Aittamaa, and John Dodds. An Analytical Model for Capillary Pressure Saturation Relation for Gas/Liquid System in a Packed-Bed of Spherical Particles. *Transport in Porous Media*, 77(1):17–40, 2008.
- [22] JM Pereira and Chloé Arson. Retention and permeability properties of damaged porous rocks. *Computers and Geotechnics*, 48:272–282, 2013.
- [23] A. Revil and L. M. Cathles. Permeability of shaly sands. *Water Resources Research*, 35(3):651, 1999.
- [24] J. a. Gili and E. E. Alonso. Microstructural deformation mechanisms of unsaturated granular soils. *International Journal for Numerical and Analytical Methods in Geomechanics*, 26(5):433–468, 2002.
- [25] T D Blake and J M Haynes. Kinetics of Liquid/Liquid Displacement. *Journal of Colloid and Interface Science*, 30(3):

- 421423, 1969.
- [26] MO Goebel and Joerg Bachmann. Water potential and aggregate size effects on contact angle and surface energy. *Soil Science Society of America Journal*, 68:383–393, 2004.
 - [27] J Bachmann, S Woche, MO Goebel, M Kirkham, and R Horton. Extended methodology for determining wetting properties of porous media. *Water Resources Research*, 39(12):1353, 2003.
 - [28] AR Russell and O Buzzi. A fractal basis for soil-water characteristics curves with hydraulic hysteresis. *Géotechnique*, 62(3):269–274, 2012.
 - [29] L. Richards. Capillary Conduction of Liquids Through Porous Mediums. *Physics*, 1(5):318, 1931.
 - [30] M van Genuchten. A Closed-form Equation for Predicting the Hydraulic Conductivity of Unsaturated Soils. *Soil Science Society of America Journal*, 44(5):892–898, 1980.
 - [31] P A Cundall and O D L Strack. A discrete numerical model for granular assemblies. *Géotechnique*, 29(1):47–65, 1979.
 - [32] M.J. Jiang, S. Leroueil, and J.M. Konrad. Insight into shear strength functions of unsaturated granulates by DEM analyses. *Computers and Geotechnics*, 31(6):473–489, 2004.
 - [33] L Scholtes, P Hicher, F Nicot, B Chareyre, and F Darve. On the capillary stress tensor in wet granular materials. *International Journal for Numerical and Analytical Methods in Geomechanics*, 33:1289–1313, 2009.
 - [34] J.-P. Gras, J.-Y. Delenne, F. Soulié, and M.S. El Youssoufi. DEM and experimental analysis of the water retention curve in polydisperse granular media. *Powder Technology*, 208(2):296–300, 2011.
 - [35] Bruno Chareyre, Andrea Cortis, and Catalano Eric Barth. Pore-scale Modeling of Viscous Flow and Induced Forces in Dense Sphere Packings. *Transport in Porous Media*, 94(2):595–615, 2012.
 - [36] Rudiger Schwarze, Anton Gladky, Fabian Uhlig, and Stefan Luding. Rheology of weakly wetted granular materials - a comparison of experimental and numerical data. *Granular Matter*, page in press, 2013.
 - [37] M. Zeghal and U. El Shamy. A continuum-discrete hydromechanical analysis of granular deposit liquefaction. *International Journal for Numerical and Analytical Methods in Geomechanics*, 28(14):1361–1383, 2004.
 - [38] Alberto Di Renzo and Francesco Paolo Di Maio. Homogeneous and bubbling fluidization regimes in DEMCFD simulations: Hydrodynamic stability of gas and liquid fluidized beds. *Chemical Engineering Science*, 62(1-2):116–130, 2007.
 - [39] Chris Rycroft, Gary Grest, James Landry, and Martin Bazant. Analysis of granular flow in a pebble-bed nuclear reactor. *Physical Review E*, 74(2):021306, 2006.
 - [40] F. Soulié, F. Cherblanc, M.S. El Youssoufi, and C. Saix. Influence of liquid bridges on the mechanical behaviour of polydisperse granular materials. *International Journal for Numerical and Analytical Methods in Geomechanics*, 30(3): 213–228, 2006.
 - [41] GC Cho and JC Santamarina. Unsaturated particulate materials-particle-level studies. *Journal of Geotechnical and Geoenvironmental Engineering*, 127:84–96, 2001.
 - [42] G. T. Houlsby. The work input to an unsaturated granular material. *Géotechnique*, 47(1):193–196, 1997.
 - [43] Federico Maggi. Multiphase capillary rise of multicomponent miscible liquids. *Colloids and Surfaces A: Physicochemical and Engineering Aspects*, 415:119–124, 2012.
 - [44] SE Powers, WH Anckner, and TF Seacord. Wettability OF NAPL-contaminated sands. *Journal of Environmental Engineering*, 122:889–896, 1996.
 - [45] Marcel G. Schaap, Mark L. Porter, Britt S. B. Christensen, and Dorte Wildenschild. Comparison of pressure-saturation characteristics derived from computed tomography and lattice Boltzmann simulations. *Water Resources Research*, 43: W12S06, 2007.